

REPORT DOCUMENTATION PAGE				Form Approved	
				OMB No. 0704-0188	
Public reporting burden for this collection of information is estimated to average 1 hour per response, including the time for reviewing instructions, searching existing data sources, gathering and maintaining the data needed, and completing and reviewing this collection of information. Send comments regarding this burden estimate or any other aspect of this collection of information, including suggestions for reducing this burden to Department of Defense, Washington Headquarters Services, Directorate for Information Operations and Reports (0704-0188), 1215 Jefferson Davis Highway, Suite 1204, Arlington, VA 22202-4302. Respondents should be aware that notwithstanding any other provision of law, no person shall be subject to any penalty for failing to comply with a collection of information if it does not display a currently valid OMB control number. PLEASE DO NOT RETURN YOUR FORM TO THE ABOVE ADDRESS.					
1. REPORT DATE 28-03-2012		2. REPORT TYPE Final Technical		3. DATES COVERED Jan 2009 to Dec 2011	
4. TITLE AND SUBTITLE Space-Based Three-Dimensional Imaging of Equatorial Plasma Bubbles: Advancing the Understanding of Ionospheric Density Depletions and Scintillation				5a. CONTRACT NUMBER	
				5b. GRANT NUMBER FA9550-09-1-0255	
				5c. PROGRAM ELEMENT NUMBER	
6. AUTHOR(S) Comberiate, Joseph M.				5d. PROJECT NUMBER	
				5e. TASK NUMBER	
				5f. WORK UNIT NUMBER	
7. PERFORMING ORGANIZATION NAME(S) AND ADDRESS(ES) Johns Hopkins University Applied Physics Laboratory 11101 Johns Hopkins Road Laurel, MD 20723				8. PERFORMING ORGANIZATION REPORT NUMBER	
9. SPONSORING / MONITORING AGENCY NAME(S) AND ADDRESS(ES) Dr. Cassandra G. Fesen 875 N Randolph St Arlington, VA 22203				10. SPONSOR/MONITOR'S ACRONYM(S)	
				11. SPONSOR/MONITOR'S REPORT NUMBER(S) afrl-osr-va-	
12. DISTRIBUTION / AVAILABILITY STATEMENT Distribution A: Approved for Public Release				tr-2012-0957	
13. SUPPLEMENTARY NOTES					
14. ABSTRACT Since their launches in October 2003 and October 2009, the SSUSI instruments on the DMSP F16 and F18 satellites have over 5 years of daily global observations of the nightside ionosphere. UV brightness observations at 135.6 nm are capable of imaging equatorial plasma bubbles. A bubble detection algorithm was applied to provide a multi-year plasma bubble climatology. A tomographic reconstruction technique was modified and applied to SSUSI data to reconstruct three-dimensional cubes of ionospheric electron density. These data cubes allowed for 3-D imaging of plasma bubbles and were used to drive HF propagation models to observe the effects of these depletions on communications. Data from the SSULI instrument on DMSP F18 was combined with SSUSI data to enhance the reconstruction, and these were validated with ALTAIR radar measurements. The relationship between SSUSI plasma bubble observations and scintillation at UHF and GPS frequencies was evaluated by scoring the correlation using ground-based scintillation data from 2006. An experimental prototype scintillation map from SSUSI observations was then developed for real-time support of warfighter communications in theater.					
15. SUBJECT TERMS					
16. SECURITY CLASSIFICATION OF:			17. LIMITATION OF ABSTRACT	18. NUMBER OF PAGES	19a. NAME OF RESPONSIBLE PERSON
a. REPORT	b. ABSTRACT	c. THIS PAGE			19b. TELEPHONE NUMBER (include area code)
U	U	U	U	30	Dr. Cassandra Fesen 703-588-8315

AFOSR Final Technical Report

Project Title: SPACE-BASED THREE-DIMENSIONAL IMAGING OF EQUATORIAL PLASMA BUBBLES

Award Number: FA9550-09-1-0255

Start Date: Jan. 1, 2009

Program Manager:

Dr. Cassandra G. Fesen
Program Manager, Space Sciences
Physics and Electronics Directorate
Air Force Office of Scientific Research
875 N Randolph St
Arlington, VA 22203
Email: cassandra.fesen@afosr.af.mil

Principal Investigator:

Dr. Joseph M. Comberiate
Johns Hopkins University Applied Physics Laboratory
Space Department
11101 Johns Hopkins Road
Laurel, MD 20723
Email: Joseph.Comberiate@jhuapl.edu
Phone: (240) 228-3177

Accomplishments/New Findings:

SSUSI provides the most extensive dataset of post-sunset plasma bubble observations. This includes a multi-year longitudinal and seasonal climatology of plasma bubble occurrence along with the dependence of bubble occurrence on solar activity.

A technique was developed to combine multiple two-dimensional altitude vs. longitude reconstructions of electron density to produce a three-dimensional electron density data cube from UV observations at 135.6 nm. These data cubes were used to evaluate differences in HF propagation characteristics in the observed ionosphere, and then compared to propagation through an ionosphere based on climatological models.

The three-dimensional reconstruction technique was expanded to incorporate both SSUSI and SSULI data from the DMSP satellite. The SSULI data provided additional observations in the along-track direction that improved the latitudinal imaging capability. Validation with ALTAIR radar data shows that the addition of the SSULI data improves the accuracy of the reconstruction.

The relationship between plasma bubbles observed by SSUSI and scintillation was established by comparisons with ground-based GPS and UHF scintillation monitors in Hawaii and Peru. Skill scores were calculated for varying regional windows to evaluate the degree of the correlation.

A tool was created to produce daily scintillation maps for a theater of interest (e.g. Afghanistan) from SSUSI data. The tool shows red areas where ground sites will experience scintillation on communications links to a satellite, yellow areas where the regions will move in the next 4 hours, and green areas where no scintillation will occur.

Summary:

Since their launches in October 2003 and October 2009, the SSUSI instruments on the DMSP F16 and F18 satellites have over 5 years of daily global observations of the nightside ionosphere. UV brightness observations at 135.6 nm are capable of imaging equatorial plasma bubbles. Equatorial plasma bubbles are regions of depleted electron density that form at low latitudes in the post-sunset ionosphere. These depleted regions typically originate in the bottomside post-sunset ionosphere and, while longitudinally thin, extend latitudinally along magnetic field lines. Sharp electron density gradients in plasma bubbles can cause significant scintillation UHF satellite communications and GPS signals. A bubble detection algorithm was applied to provide a multi-year plasma bubble climatology. A tomographic reconstruction technique was modified and applied to SSUSI data to reconstruct three-dimensional cubes of ionospheric electron density. These data cubes allowed for 3-D imaging of plasma bubbles and were used to drive HF propagation models to observe the effects of these depletions on communications. Data from the SSUSI instrument on DMSP F18 was combined with SSUSI data to enhance these reconstructions, which were validated using ALTAIR radar measurements. The relationship between SSUSI plasma bubble observations and scintillation at UHF and GPS frequencies was evaluated by scoring the correlation of ground-based scintillation data from 2006. An experimental prototype scintillation map from SSUSI observations was then developed for real-time support of warfighters in theater.

Bubble Climatology

Since its launch in October 2003, the SSUSI instrument on the DMSP F16 satellite has over 5 years of daily global observations of the nightside ionosphere. Equatorial plasma bubbles are regions of depleted electron density that form at low latitudes in the post-sunset ionosphere. These depleted regions typically originate in the bottomside post-sunset ionosphere and, while longitudinally thin, extend latitudinally along magnetic field lines. Sharp electron density gradients in plasma bubbles can cause significant scintillation UHF satellite communications and GPS signals. The bubble detection algorithm described in *Comberiate and Paxton* [2010] was used to create a plasma bubble climatology at 20 LT. Figure 1 shows the yearly plasma bubble occurrence rate along with the international sunspot number. From 2004 through 2007, the decline in bubble occurrence rate mirrors the decline in sunspot number. However, the bubble occurrence rate reaches a floor from 2007 to 2008.

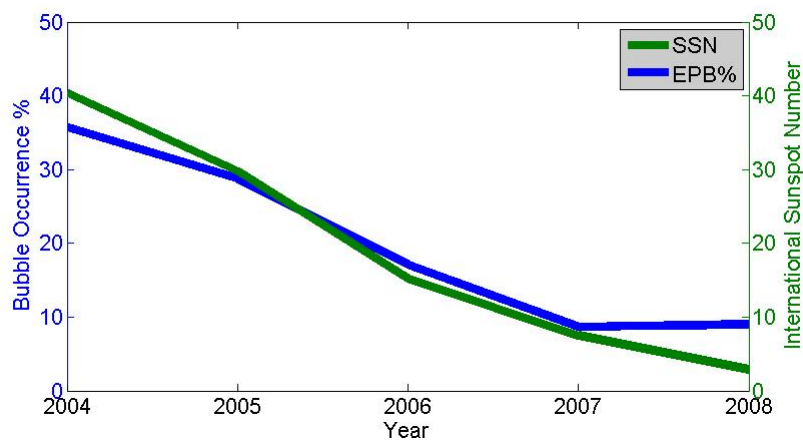


Figure 1: Bubble occurrence percentage and sunspot number from 2004-2008. Plasma bubble occurrence decreases with decreasing solar activity.

In order to evaluate the longitudinal and seasonal effects on plasma bubble occurrence, orbits were divided into six longitude sectors (spanning 60° each) and the year was divided into six two-month intervals. Figure 2 shows plots of the seasonal and longitudinal variability of plasma bubble occurrence. Overall from 2004 through 2008, plasma bubbles were detected on 2,192 of 13,287 orbits, an occurrence rate of 16.5%. Equatorial plasma bubble occurrence is enhanced during the Atlantic northern winter, Indian equinox, and Pacific equinox periods. These results are consistent with past studies [*Maruyama and Matuura, 1984*]. Overall EPB occurrence rates are greatest in equinoctial periods, and lowest near solstices. The exception is in the Brazilian sector, where plasma bubble occurrence is highest between September and December. These trends are consistent with the work of *Tsunoda* [1985], who suggested that plasma bubble occurrence rates should be highest when the angle between the day-night terminator and magnetic flux tubes approaches 0° . This ensures that the *E*-region conductivity on both sides of the flux tube is minimal, since one side of the flux tube remain sunlit would increase the flux-tube integrated *E*-region conductivity and thereby inhibit the growth of the Rayleigh-Taylor instability [*Sultan 1996*]. The curvature in the magnetic equator in the Brazilian sector and the corresponding variation in plasma bubble occurrence supports this explanation.

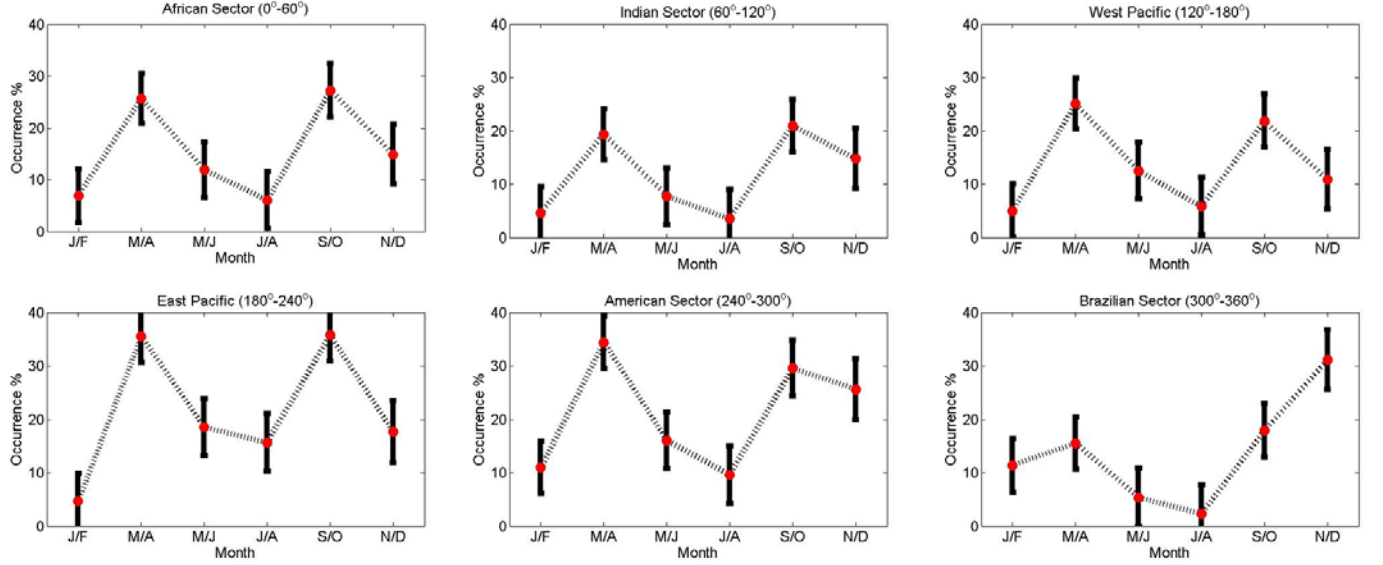


Figure 2: Seasonal/longitudinal variations of plasma bubble activity at 20 LT. Peak activity is during equinoctial periods for most longitudes except for a peak in November/December in the Brazilian sector.

3-D Plasma Bubble Imaging

Since SSUSI orbits at 830 km and has a 140° cross-track scan, its line of sight brightness observations provide both longitude and altitude information. UV brightness at 135.6 nm is proportional to the square of the electron density integrated along the line of sight. A discrete forward model of the SSUSI observations can be constructed in the following form:

$$\mathbf{y} \text{ (Rayleighs)} = \frac{7.3 \times 10^{-13} \text{ cm}^3 \text{ s}^{-1}}{10^6 \text{ photons cm}^{-2} \text{ s}^{-1}} \frac{10^5 \text{ cm}}{\text{km}} \mathbf{A}(\text{km}) \mathbf{x}(\text{cm}^{-6}) \quad (2)$$

where \mathbf{y} is an array of SSUSI 135.6 nm brightness measurements, \mathbf{x} is an array of discrete ionospheric voxels with constant values for the squared electron density, and \mathbf{A} is a matrix where the values $A(i,j)$ are the lengths of the line of sight for observation i contained in the ionospheric voxel j [Comberiate et al., 2007].

Successive SSUSI disk scans provide overlapping line-of-sight observations spanning a three-dimensional segment of the ionosphere. If the segment of the ionosphere is assumed to be constant with respect to magnetic field lines over an approximately 10° latitude window (11 cross-track scans of the SSUSI instrument), the electron density reconstruction from SSUSI measurements reduces to a 2-D tomographic inversion problem. For each of these segments (spanning 10° latitude), a tomographic inversion is performed to reconstruct an altitude vs. longitude electron density cross-section.

The tomographic inversion algorithm is a method for solving for the unknown ionosphere x in Eq. 1. Details of the tomographic reconstruction algorithm are described in *Comberiate et al.* [2007]. Additional cross-sections are reconstructed at 6.4° latitude intervals (five cross-track scans span 6.4° latitude), such that 12 slices are combined to form a three-dimensional electron density profile. Since each slice uses 11 cross-track scans, spacing at 6.4° latitude intervals means that roughly half of the data used to reconstruct one cross-section will also be used in the successive cross-section. The reconstructed three-dimensional electron density grid has 6.4° latitude resolution, 0.33° longitude resolution, and 20 km altitude resolution. It is possible to improve the latitude resolution by running the inversion algorithm at smaller intervals, down to 1.3° latitude.

There are several limitations to this electron density data cube reconstruction approach that are sources of error in the reconstructed density values. The major source of error is the statistical error from the low number of photon counts in the observation. *Comberiate* [2007] presents an

analysis of statistical error based on a Gaussian noise model. When there are insufficient counts (< 10 counts) to model the Poisson counting process as Gaussian, reconstructed electron density values may be biased high. This will often occur during solar minimum conditions. The limited angle viewing geometry results in higher statistical error towards the edges of the data cube. There is also an inherent difficulty in the use of this tomographic reconstruction technique to resolve the latitudinal structure of the ionosphere. The assumption that the ionosphere is invariant with respect to magnetic field lines over a 10° latitude span leads to smearing of latitudinally varying features in the reconstructed data cube. Despite these limitations, the three-dimensional electron density map is still able to capture the structure of the enhanced electron density in the equatorial arcs and provide images of the large-scale structure of plasma bubbles. Figure 3 shows an example of a three-dimensional reconstruction of a plasma bubble and the 3-D background ionospheric electron density profile from different vantage points.

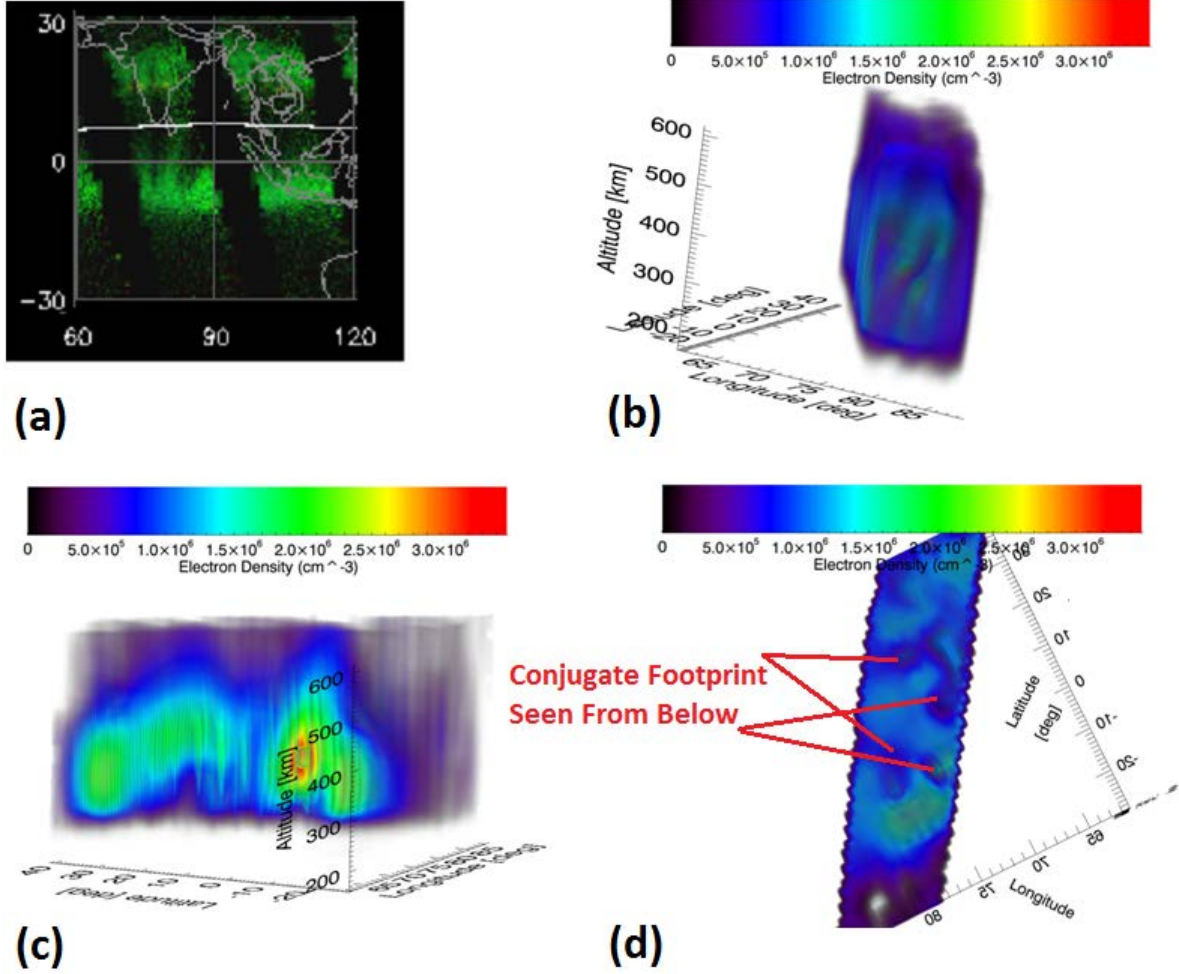


Figure 3: Multiple views of a three-dimensional reconstruction of plasma bubbles. (a) Summary image view of 135.6 nm brightness with depletion signatures over India. (b) North-looking view showing bubbles branching in longitude with increasing altitude. (c) East-looking view showing the variations in the height profile and peak densities of the background ionosphere with latitude. (d) Upward-looking view showing the conjugate footprints of the bubbles.

Effects on HF Propagation

Since the electron density reconstruction is a three-dimensional data cube, SSUSI data can drive an HF propagation model. The SSUSI data is input as a three dimensional grid of electron density values at geodetic latitude, longitude and altitude grid positions and regridded to geomagnetic coordinates, the computational coordinate system used by the ray tracing algorithm.

The electron density between grid points is calculated using three dimensional linear interpolation. The radio propagation model used in this study is based on the Jones-Stephenson ray tracing algorithm outlined in *Jones & Stephenson* [1975]. Likewise, for comparison of results from ray tracing through the SSUSI reconstructions with a climatology-based electron density model, we have incorporated IRI-2001 output into the ray tracing code in a similar manner.

In Figure 4 we show an example of 25 MHz HF ray tracing results through a slice of the SSUSI reconstruction and the IRI-2001 model. In this case, the O-mode or ordinary ray was launched north along 20° longitude and intersected a bubble. In the SSUSI data that caused anomalous refraction for rays launched between 20° and 30° elevation. One ray in particular intersects the top edge of the bubble, bending the ray back toward the right edge of the bubble and returning to the ground at a greater range than any of the other elevation ray paths. In a smooth ionosphere, this ray would have penetrated the ionosphere as did the rays alongside. Also, the SSUSI reconstruction shows higher peak plasma frequency – 15 MHz compared to 11 MHz in the IRI-2001 model – in the equatorial arcs, allowing for all but the lowest elevation rays to penetrate the ionosphere in the IRI-2001 model. This type of analysis using the HF propagation model can also be used to estimate the Maximum Usable Frequency (MUF) for a given ground range.

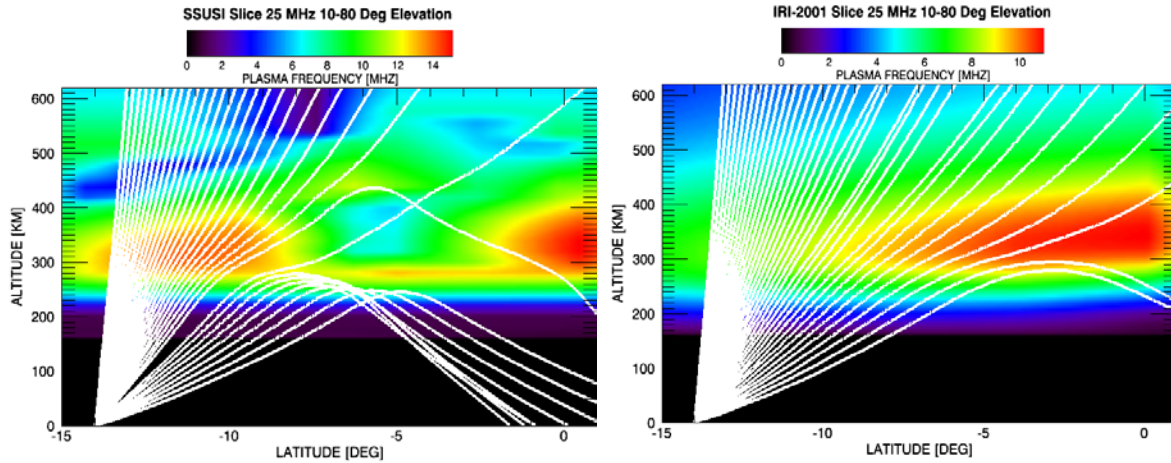


Figure 4. Comparison of sample ray tracing through SSUSI reconstruction (left) and IRI-2001 model (right). The color contours show the plasma frequency (electron density) profile in a two dimensional slice through the reconstruction and model. Both ray tracing runs were completed using 25 MHz carrier frequency from the same geographic location, scanning initial elevation angles of 10°-80° at 2° steps.

Multi-Instrument 3-D Imaging

A joint SSUSI/SSULI 3-D electron density reconstruction algorithm was developed to evaluate if 3-D electron density gradients were a significant source of error that could be reduced with a new data source. This algorithm builds on previous tomographic algorithms that reconstruct electron density from SSUSI 135.6 nm UV radiance data. The tomographic approach reconstructs two-dimensional altitude vs. longitude grid by applying an algebraic reconstruction technique to 11 consecutive SSUSI cross-track scans, and by assuming the ionosphere is invariant in the third dimension. A three-dimensional reconstruction approach would capture variations along the orbit track by using SSULI data. However, even with both the SSUSI and SSULI instruments taking observations, there is not enough overlapping data to support reconstruction of a full three-dimensional volume. A series of two-dimensional cross-sections were reconstructed instead. These two-dimensional altitude vs. longitude cross-sections are

reconstructed once for every five SSUSI scans and stacked along the orbit track to create a three-dimensional ionosphere. The dual challenges of this approach are how to use data from the perpendicular SSUSI and SSULI observation planes simultaneously for two-dimensional reconstructions and how to preserve the strength of each instrument's dataset so that combined reconstruction is an improvement over independent reconstructions. The solution is to use an iterative reconstruction approach, that is tightly constrained by previous iterations through projection onto convex sets.

This approach is implemented in three phases:

Phase 1: Reconstruct 3-D data cube using only SSUSI data

The 3-D data cube is a 12x24x30 (lat/alt/lon) grid with 6° latitude resolution (approximately 1.2° per scan), 20 km altitude resolution, and 0.33° longitude resolution. The data cube is created from a series of 2-D cross-sections reconstructed using 11 cross-track scans of SSUSI data each, staggered every five scans. The spatial pixels for each scan are binned to improve the counting statistics. (This is the same approach described earlier in the report.)

Phase 2: Reconstruct 2-D along-track cross-sections using SSULI data, constrained by SSUSI reconstruction.

A 2-D reconstruction is performed over the same latitude span as the SSUSI 3D reconstruction. The same tomographic imaging technique is used with SSULI observations in the orbit plane. Because a single SSULI line-of-sight observation can look through up to 25° of latitude, the 5° latitude resolution of the 3-D grid is also appropriate for the SSULI reconstruction. In order to ensure full coverage of the grid with SSULI lines of sight, the reconstruction is initially

performed for a larger grid and additional SSULI satellite positions. The SSULI lines-of-sight do not have complete coverage of the edges of the grid so the edges of the grid that are outside of the region of interest are truncated. Limb scans however do support high-resolution altitude profiles so the 20 km altitude resolution for the reconstruction grid is appropriate. In short, SSULI data is used to reconstruct the center 2-D slice (altitude vs. orbit track) of the 3-D reconstruction. This slice provides a single altitude profile constraint for each of the multiple SSUSI reconstructions in a perpendicular direction.

Phase 3: Reconstruct 3D data cube again, constrained by SSULI reconstruction

The third phase of the reconstruction technique is the reconstruct the 3-D data cube again, this time using the SSULI reconstruction as a strict constraint (enforced by projection onto convex sets) instead of the generic PIM model ionosphere used in Phase 1. The SSULI reference image provides a more accurate latitudinal structure of the ionosphere than the initial SSUSI image and also enhances the altitude profile.

Validation:

Reconstructions using the SSUSI/SSULI algorithm were validated by comparison to ground truth data from the ALTAIR radar. For each overflight, the ALTAIR radar took two scans. The first scan was in the along-track direction, corresponding to the SSULI field of view. The second scan was in the cross-track direction, corresponding to the SSUSI field of view. This provided two perpendicular cross-sections that could be used to validate the SSUSI/SSULI combined 3D data cube.

Validation was performed with ALTAIR data from Apr 6, Jul 24, Jul 25, Aug 1, Aug 19, Aug 26, and Aug 27, 2010. These are the same scans that were used for SSULI validation. ALTAIR data were binned and interpolated to match the SSUSI/SSULI reconstruction grid. hmF2 and NmF2 were compared for every vertical column where there were valid data points from both sources. NmF2 was the peak electron density value in the vertical column and hmF2 was the height of that value. For the SSUSI and SSULI comparisons to follow, the longitude segment corresponds to SSUSI and the latitude segment corresponds to SSULI. ALTAIR electron density values outside of the range $[1\text{e}4\text{-}3\text{e}6\text{ cm}^{-3}]$ were excluded. hmF2 values were restricted to a range of 240-500 km. NmF2 values were restricted to a range of $[1\text{e}5\text{-}3\text{e}6\text{ cm}^{-3}]$. Electron density values were compared at every point where the DMSP reconstruction overlapped with the ALTAIR data.

After the initial validation analysis, a change was made to the SSUSI/SSULI forward model to correct for the contribution of mutual neutralization to the 135.6 nm emission. The correction used an altitude-dependent value of $\alpha_{135.6}$ over the altitude range of 150-370 km. $\alpha_{135.6}$ increased linearly from $4.0 \times 10^{-13}\text{ cm}^3\text{s}^{-1}$ at 150 km to $7.3 \times 10^{-13}\text{ cm}^3\text{s}^{-1}$ at 370 km. Above 370 km, $\alpha_{135.6}$ was fixed at $7.3 \times 10^{-13}\text{ cm}^3\text{s}^{-1}$.

Figure 5 shows the hmF2 validation for the combined reconstruction versus ALTAIR hmF2, both in the SSULI observation plane and in the SSUSI observation plane. Figure 6 identifies an expected error of 47 km and a threshold of $6\text{e}5\text{ cm}^{-3}$ for hmF2 determination. Figure 7 shows the NmF2 validation for the combined reconstruction versus ALTAIR hmF2, both in the SSULI

observation plane and in the SSUSI observation plane. Figure 8 identifies an expected fractional error of 27% and a threshold of $6e5 \text{ cm}^{-3}$ for NmF2 determination. Figure 9 shows the Ne validation for the combined reconstruction versus ALTAIR hmF2, both in the SSULI observation plane and in the SSUSI observation plane. Figure 10 identifies an expected fractional error of 42% and a threshold of $4e5 \text{ cm}^{-3}$ for NmF2 determination. These validations were performed for solar minimum conditions and the algorithms are likely to perform better under solar maximum conditions with higher ionospheric electron densities, as the SNR of the 135.6 nm observations are higher with a brighter ionosphere.

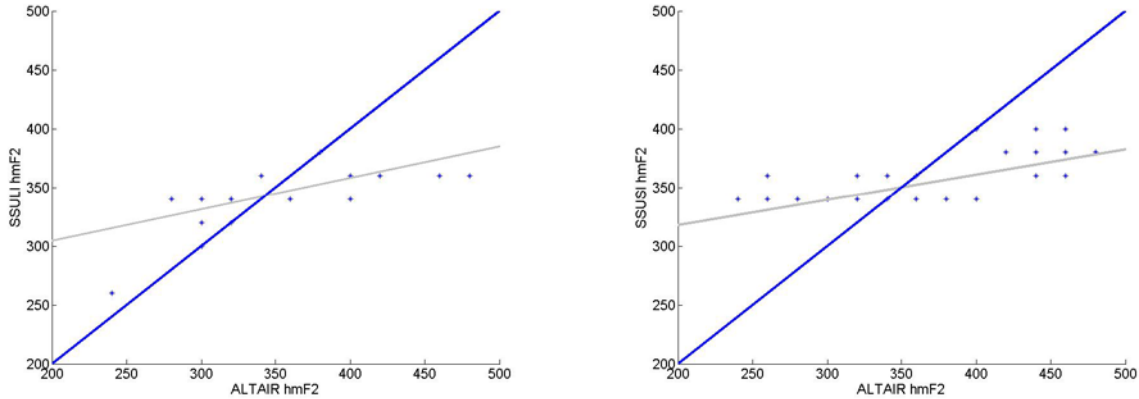


Figure 5. HmF2 validation: Left panel: SSULI-ALTAIR hmF2, $\mu = -6 \text{ km}$, $\sigma = 45 \text{ km}$. Right panel: SSUSI-ALTAIR hmF2, $\mu = 5 \text{ km}$, $\sigma = 48 \text{ km}$. μ refers to the mean difference between the DMSP and ALTAIR values and σ is the standard deviation of the discrepancy between the two values. The blue line is the line of perfect agreement and the grey line is the least squares “best fit” line to the data.

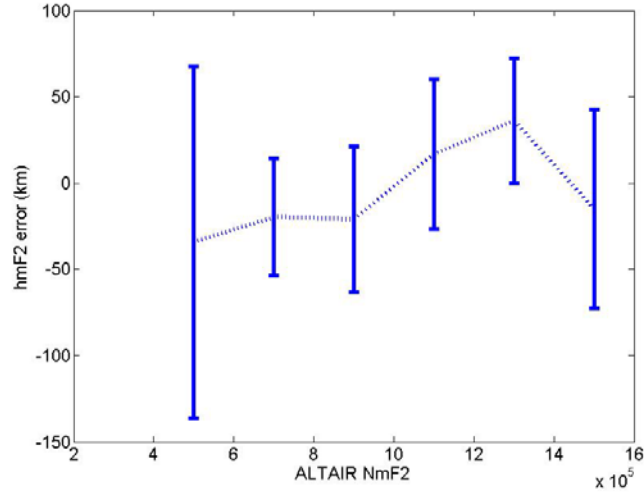


Figure 6. *hmF2 validation: Expected error of 47 km above threshold of $6e5 \text{ cm}^{-3}$. The standard deviation of the combined error above the threshold is 48 km and the RMS error above the threshold is also 48 km.*

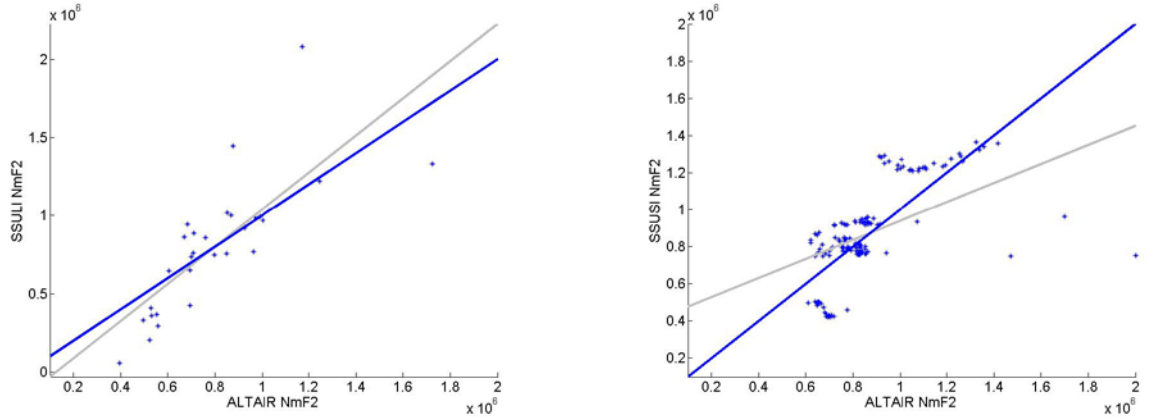


Figure 7. *NmF2 Validation. left panel: SSULI-ALTAIR NmF2, $\mu = 6.4e2$, $\sigma = 2.7e5$. Right panel: SSUSI-ALTAIR NmF2 $\mu = 1.5e3$ $\sigma = 2.5e5$. μ refers to the mean difference between the DMSP and ALTAIR values and σ is the standard deviation of the discrepancy between the two values. The blue line is the line of perfect agreement and the grey line is the least squares “best fit” line to the data.*

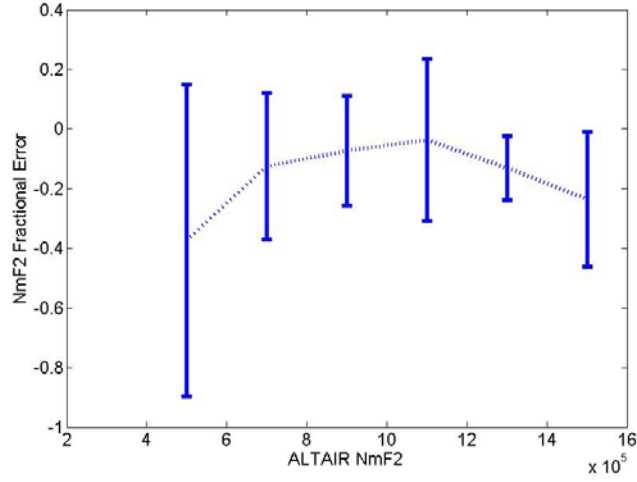


Figure 8. Fractional error standard deviation below 27% for NmF2 above $6e5 \text{ cm}^{-3}$. The standard deviation of the combined fractional error above the threshold is 22% and the RMS fractional error above the threshold is also 22%.

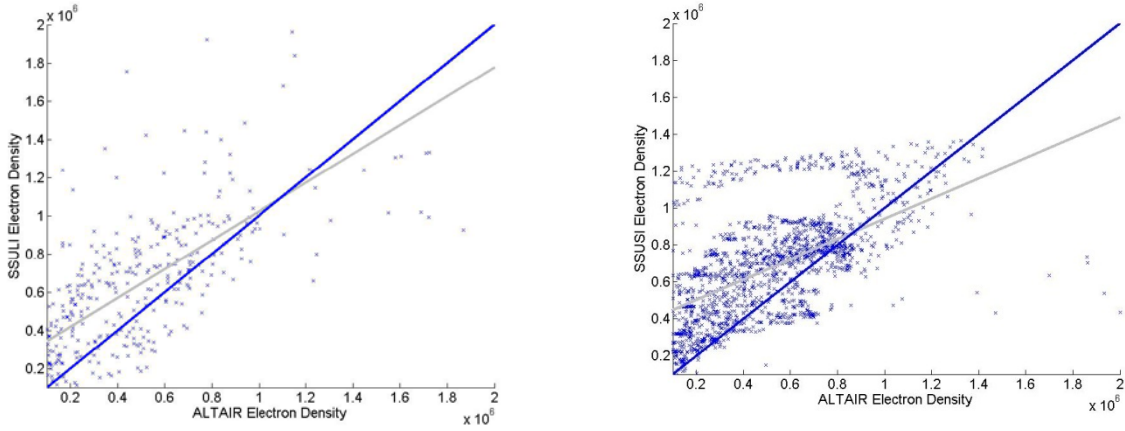


Figure 9. Electron Density Validation. Left panel: SSULI-ALTAIR Ne $\mu = -1.4e5$ $\sigma = 3.0e5$. Right panel: SSUSI-ALTAIR Ne $\mu = -1.6e5$ $\sigma = 2.7e5$. μ refers to the mean difference between the DMSP and ALTAIR values and σ is the standard deviation of the discrepancy between the two values. The blue line is the line of perfect agreement and the grey line is the least squares “best fit” line to the data.

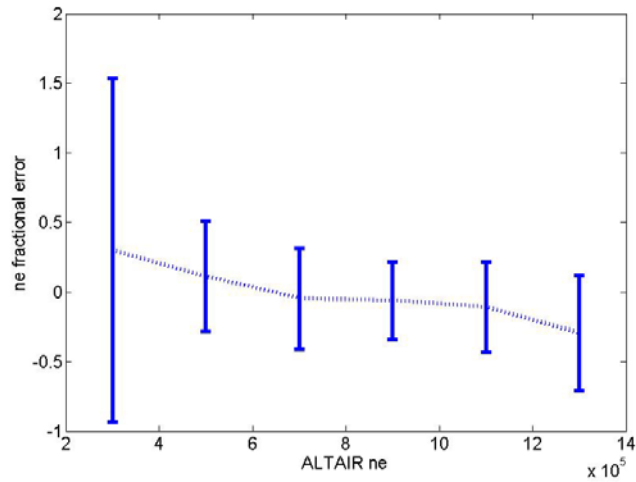


Figure 10. Fractional error standard deviation below 42% for Ne above $4e5 \text{ cm}^{-3}$. The standard deviation of the combined error above the threshold is 40% and the RMS error above the threshold is 44%.

Relating Bubbles and Scintillation

While plasma bubbles are typically associated with scintillation, the nature of the relationship between plasma depletions observed by UV imaging satellites and observed scintillation at GPS and UHF-SATCOM frequencies has not been thoroughly explored. In order to score the ability of bubble observations to predict various levels of scintillation, coincident observations between SSUSI and ground-based scintillation monitors were studied. The AFRL SCINDA (SCINTillation Network Decision Aid) station at Ancón, Perú (geog. 11.79° S, 77.18° W; mag. 0.5° N, 5.31° W), is designed to monitor UHF-SATCOM (250 MHz) signals from geostationary spacecraft for scintillation. This station looks at two different UHF satellites to provide a West and an East observation of scintillation. A Cornell University Scintillation Monitor (ScintMon; now operated jointly by the University of Illinois and Cornell) is located on Mt. Haleakla, Hawaii. It receives GPS L1 (1.57542 GHz) signals from GPS satellites above 15° elevation.

Direct coincidences between SSUSI bubble observations and the ground-based sites were rare, so some assumptions were made to provide a comparison window. Bubbles were assumed to extend along magnetic field lines. We expect bubbles to drift Eastward over ground sites and cause scintillation, so we evaluated bubbles in a 12° magnetic longitude window around the ground-based site and looked for corresponding S4 above a specified threshold between 7 PM and 1 AM local time.

The comparisons were scored as follows:

S4	Y	a	c
	N	b	d
		Y	N
		bubble	

The Peirce Skill Score (PSS) is an equitable skill score that can provide a metric of the success of predicting scintillation from bubble observations. The range of values for the PSS are from +1 (perfect predictor) to -1, with a score of 0 indicating no skill. An effective predictor will have a positive skill score.

$$PSS = (ad-bc)/(a+c)(b+d)$$

Scintillation data was available from 2006 and was compared with bubble observations from the SSUSI F16 satellite.

The first comparison was made with the 2006 ScintMon GPS data, using a threshold of $S4 > 0.10$.

Figure 11 is a graphical representation of the results.

S4	Y	17	24
	N	28	135
		Y	N
		Bubble	

PSS = 0.24

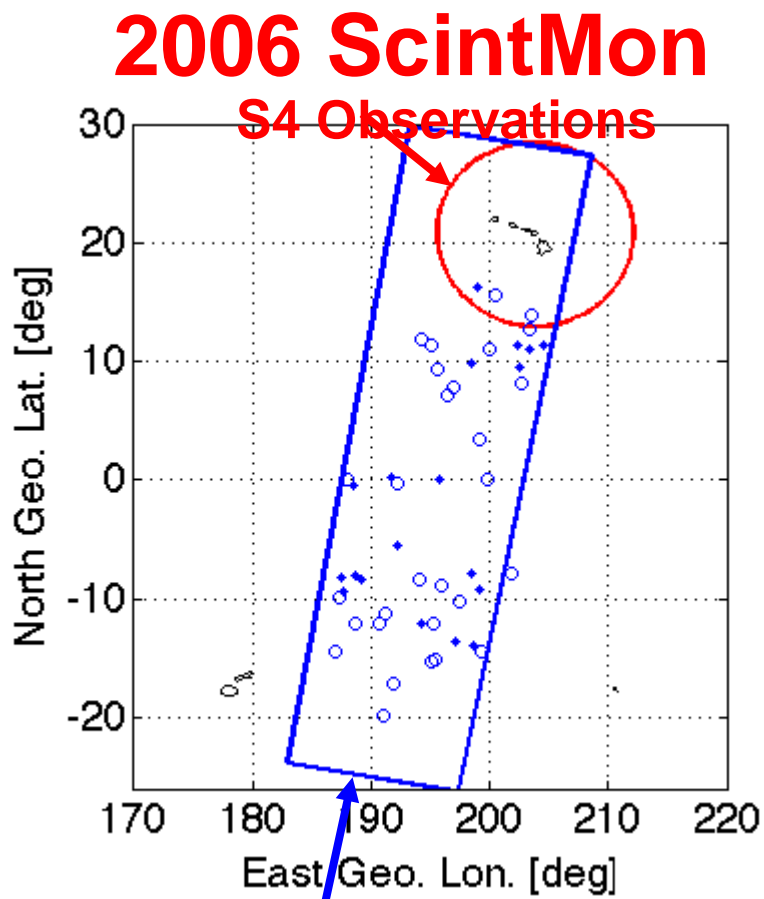


Figure 11: Comparison of observed bubble detections with ScintMon GPS S4 observations. Solid circles are locations of bubble detections that corresponded with $S4 > 0.1$, hollow circles are locations of bubble detections without $S4 < 0.1$. Blue box is the bubble detection window and red circle is the S4 observation window.

The next comparison was for UHF SATCOM 250 MHz scintillation, with thresholds of $S4 > 0.25$ and $S4 > 0.50$. Figure 12 shows a graphical representation of the results for the SCINDA UHF EAST detector with $S4 > 0.50$ threshold.

SCINDA UHF WEST, $S4 > 0.25$

S4	Y	13	67
	N	9	78
		Y	N
		Bubble	

PSS = 0.06

SCINDA UHF EAST, $S4 > 0.25$

S4	Y	15	80
	N	7	65
		Y	N
		Bubble	

PSS = 0.06

SCINDA UHF WEST, $S4 > 0.50$

S4	Y	9	33
	N	13	112
		Y	N
		Bubble	

PSS = 0.11

SCINDA UHF WEST, $S4 > 0.50$

S4	Y	14	47
	N	8	98
		Y	N

Bubble

PSS = 0.15

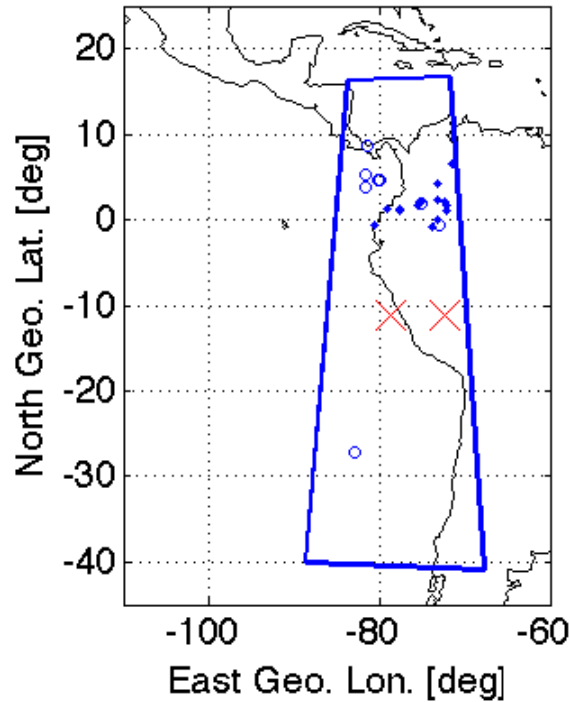


Figure 12: Comparison of observed bubble detections with SCINDA UHF S4 observations. Solid circles are locations of bubble detections that corresponded with $S4 > 0.25$ for the SCINDA UHF East station, hollow circles are locations of bubble detections without $S4 < 0.25$. Blue box is the bubble detection window and each red X is a SCINDA UHF site.

In order to evaluate the effects of the size of the window on the bubble/scintillation relationship, a narrower subset of data was evaluated. Bubbles were detected in a 3° magnetic longitude window to the West of the SCINDA UHF EAST site and checked against corresponding S4 above the threshold between 20 LT and 23 LT. In this case, $S4 > 0.25$ was observed for 86% of bubbles and skill scores significantly increased, albeit over a small sample size.

SCINDA UHF EAST, $S4 > 0.25$

S4	Y	6	14
	N	1	11

Y N
Bubble

PSS = 0.22

SCINDA UHF EAST, S4 > 0.50

S4	Y	4	7
	N	3	18
	Y		N

Bubble

PSS = 0.22

A final investigation was conducted to determine if the characteristics of the equatorial arcs seen by SSUSI could provide additional capability for specifying severe scintillation. A detection scheme would predict scintillation if any of following criteria were met:

1. Bubble seen by SSUSI
2. Separation between arcs = 15°-25° or >50°
3. North/South electron density ratio below 2

For the original comparison window, the following results were achieved:

SCINDA UHF WEST, S4 > 0.50

S4	Y	24	17
	N	34	60
	Y		N

Bubble

PSS = 0.22 (up from 0.11)

SCINDA UHF EAST, S4 > 0.50

S4	Y	32	23
	N	26	54

Y N Bubble

PSS = 0.26 (up from 0.15)

Scintillation Maps

An experimental prototype of daily scintillation maps from SSUSI F18 data is currently being field tested with an 82nd Airborne unit deployed in Afghanistan. The scintillation map is derived from the three-dimensional electron density data cube.

Once the data cube is produced for the region, the bubble regions are identified. Anomaly regions are identified as any depletion region between 230 km and 510 km in altitude that is more than two standard deviations below the mean electron density value in the data cube at that altitude (excluding the 5 lowest electron density values). The depleted pixels must have at least three neighboring depleted pixels to be large enough to be considered a real anomaly.

After the anomaly regions are determined, the 3-D cube is mapped to the ground from a satellite at a specified longitude (e.g. 80°) in geostationary orbit. A grid with 1° latitude resolution and 1/3° longitude resolution on the ground has lines of sight going to the specified satellite location.

Any point in the grid with a line of sight passing through an anomaly region is colored red.

Areas to the east of the red regions are colored yellow (if not already red) and all other regions with lines of sight that pass through the 3-D electron density cube are colored green. The map can be generated for any longitude sector once a day. Field testing will compare observed UHF SATCOM scintillation and outages with the predictions from the SSUSI maps. This testing will verify that SSUSI is identifying scintillation regions and specifying their boundaries properly.

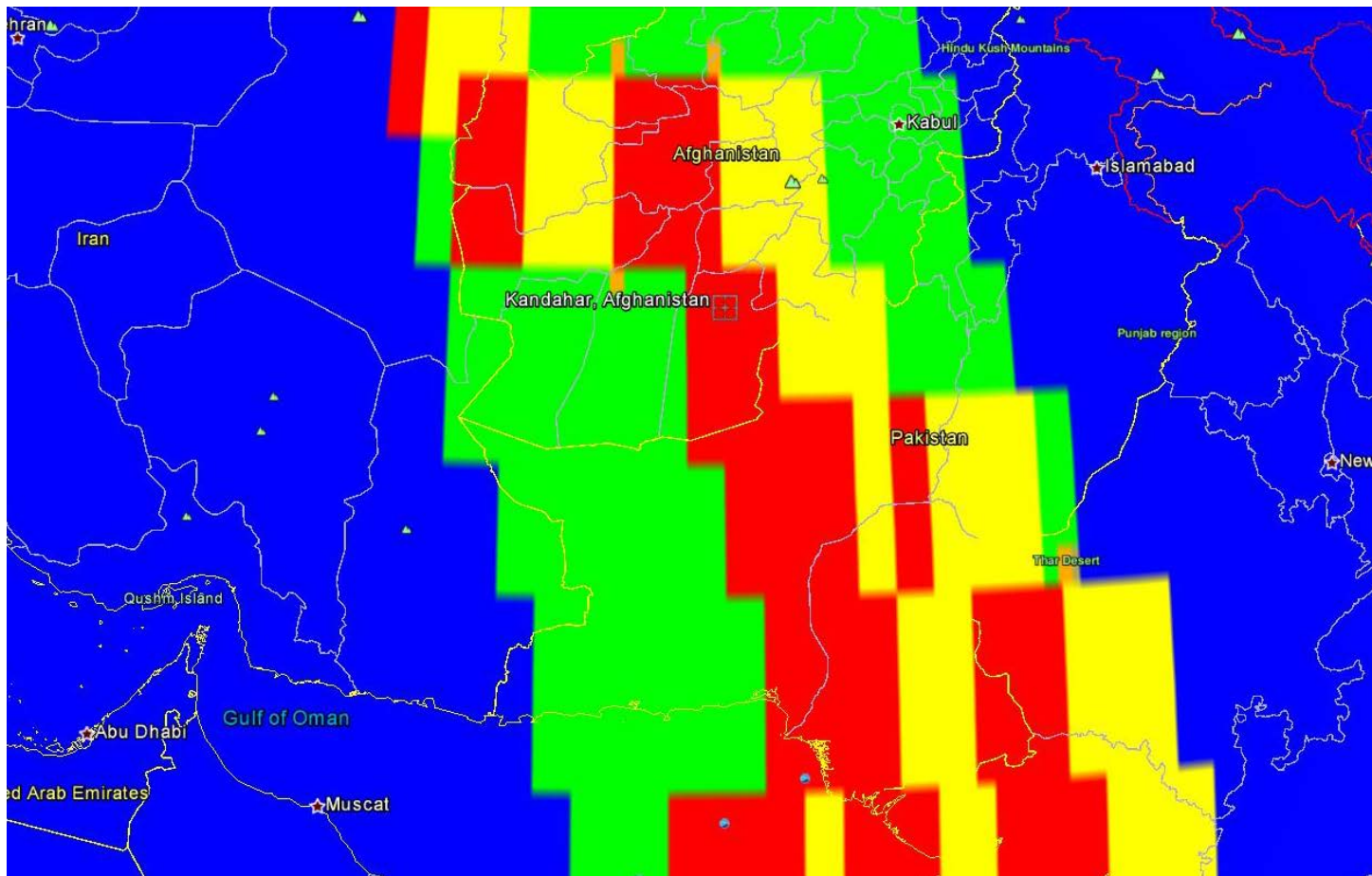


Figure 13: Scintillation map for Afghanistan theater on 10/16/2011. Red areas are current scintillation regions, yellow areas are regions with scintillation expected in the next 4 hours, green areas are quiet regions, and blue areas do not have any SSUSI data.

References

- Comberiate, J. M., F. Kamalabadi, and L. J. Paxton (2007), A tomographic model for ionospheric imaging with the Global Ultraviolet Imager, *Radio Sci.*, 42, RS2011, doi:10.1029/2005RS003348.
- Comberiate, J., and L. J. Paxton (2010), Global Ultraviolet Imager equatorial plasma bubble imaging and climatology, 2002–2007, *J. Geophys. Res.*, 115, A04305, doi:10.1029/2009JA014707.
- Jones, R. M. and J. J. Stephenson (1975), A Versatile Three-Dimensional Ray Tracing Computer Program for Radio Waves in the Ionosphere, U.S. Dept. of Commerce Office of Telecommunications Report, 75-76.
- Maruyama, T. and N. Matuura (1984), Longitudinal variability of annual changes in activity of equatorial spread F and plasma bubbles, *Journal of Geophysical Research*, 89, 10903-10912.
- Sultan, P. J., Linear theory and modeling of the Rayleigh-Taylor instability leading to the occurrence of equatorial spread F , *Journal of Geophysical Research*, 101, 26875-26891, 1996.
- Tsunoda, R. T., Control of the seasonal and longitudinal occurrence of equatorial scintillations by the longitudinal gradient in integrated E region Pedersen conductivity, *Journal of Geophysical Research*, 90, 447-456, 1985.

Personnel:

Dr. Joseph M. Comberiate (JHU/APL)

Publications (supported by this grant):

Comberiate, J., and L. J. Paxton (2010), Global Ultraviolet Imager equatorial plasma bubble imaging and climatology, 2002–2007, *J. Geophys. Res.*, 115, A04305, doi:10.1029/2009JA014707.

Comberiate, J., and L. J. Paxton (2010), Coordinated UV imaging of equatorial plasma bubbles using TIMED/GUVI and DMSP/SSUSI, *Space Weather*, 8, S10002, doi:10.1029/2009SW000546.

Interactions (supported by this grant):2011

Comberiate, J. M., E. S. Miller, L. J. Paxton, C. M. Selby, J. J. Makela, Coordinated Observations of Equatorial Plasma Bubbles, Ionospheric Drift Rates, and Scintillation, AGU Chapman Conference on Modeling the Ionosphere/Thermosphere System, Charleston, South Carolina, May 8-12, 2011.

Comberiate, J. M., E. M. Taylor, M. Reilly, L. J. Paxton, and E. S. Miller, Exploitation of DMSP/SSUSI Data for HF Applications and GPS Scintillation Forecasting, Ionospheric Effects Symposium, Alexandria, Virginia, May 18-19, 2011.

Comberiate, J. M., 3-D Reconstruction of Plasma Bubbles with DMSP/SSUSI for HF Applications and Scintillation Forecasting, Air Force Space Science Review, Albuquerque, New Mexico, June 23-24, 2011.

Comberiate, J. M., L. J. Paxton, and E. S. Miller, Scintillation Prediction from DMSP/SSUSI UV Observations, CEDAR 2011 Conference, Santa Fe, New Mexico, June 27-July 1, 2011.

Comberiate, J.M., E.M. Taylor, M.A. Kelly, L.J. Paxton, E.S. Miller, DMSP/SSUSI 3D Electron Density Maps as a Tool for UHF SATCOM Scintillation Forecasting, AMOS 2011 Conference, Maui, Hawaii, September 12-13, 2011.

2010

Comberiate, J. M., L. J. Paxton, E. M. Taylor, and C. M. Selby, Global Morphology and Climatology of Ionospheric Irregularities from DMSP/SSUSI Observations, Air Force ORION Conference, Dayton, Ohio, January 12-14, 2010.

Comberiate, J.M., E.M. Taylor, M. Reilly, M. Kelly, and L. Paxton, Exploitation of DMSP/SSUSI Data for HF Applications, SEASONS 2010 Conference, Laurel, MD, November 3-4, 2010.

2009

Comberiate, J. M., L. J. Paxton, M. Paul, and M. Kelly, AURORA: A Cost Effective Solution to Monitoring, Imaging, and Forecasting Low Latitude Ionospheric Irregularities, Space Weather Workshop 2009, Boulder, Colorado, April 28 – May 1, 2009.

Comberiate, J. M. and L. J. Paxton, Coordinated Space-Based Observations of Equatorial Plasma Bubbles Using TIMED/GUVI and DMSP/SSUSI, CEDAR 2009, Santa Fe, New Mexico, June 30, 2009.

Comberiate, J. M. and L. J. Paxton, Coordinated Space-Based Observations of Equatorial Plasma Bubbles Using TIMED/GUVI and DMSP/SSUSI, AIAA Region I Young Professional, Student and Education Conference, Laurel, Maryland, November 6, 2009.

Comberiate, J. M., E. S. Miller, L. J. Paxton, and J. Makela, Coordinated Ground- and Space-based 3-D Electron Density Reconstruction and Plasma Bubble Imaging, American Geophysical Union Fall 2009 Meeting, San Francisco, CA, December 14-18, 2009.